Journal of Materials Chemistry A

PAPER

View Article Online
View Journal | View Issue

Cite this: J. Mater. Chem. A, 2017, 5, 24168

Colloidal engineering for monolayer $CH_3NH_3PbI_3$ films toward high performance perovskite solar cells†

Bo Li,[a] Mengjie Li,[a] Chengbin Fei,[b] Guozhong Cao [ac] and Jianjun Tian *[a]

Received 4th October 2017
Accepted 1st November 2017

DOI: 10.1039/c7ta08761f

rsc.li/materials-a

It is very significant to understand the formation of perovskite crystals from the precursor solution and construct high-quality films to achieve highly efficient perovskite solar cells (PSCs). Here, we have revealed a colloidal strategy to prepare compact monolayer perovskite films by controlling the size of colloidal clusters in the perovskite precursor. Under the action of the coordination interaction, the introduction of CH_3NH_3Cl (MACl) into the standard perovskite precursor significantly increases the size of colloidal clusters. Meanwhile, *N*-dimethyl sulfoxide (DMSO) is further employed to stabilize the characteristics of the colloidal clusters and improve the reproducibility of the anti-solvent method. The large colloidal clusters can be orderly arranged on the substrate by spin-coating to form intermediate phase monolayer films, which grow to form large grains with an average size of 3 μm. Due to the much lower trap-state density and higher crystallinity of the monolayer perovskite films, a power conversion efficiency (PCE) of 19.14% has been achieved. This study sheds light on the conversion mechanism of perovskite crystals from the colloidal precursor to solid films, and paves the way for further improvement of high-quality perovskite films that can lead to high performance devices.

Introduction

Organic–inorganic hybrid perovskite solar cells (PSCs) have recently attracted enormous interest with power conversion efficiency (PCE) rising from 3.81% to over 20%.[1,2] Such rapid evolution of PCE is mainly attributed to the strong optical absorption, low exciton binding energy, long free carrier diffusion length and unique defect tolerance of organic–inorganic hybrid perovskite materials.[3–5] As one of the advantages for PSCs, organic–inorganic hybrid perovskite films can be prepared by cost effective methods, such as low temperature solution processes.[6,7] For solution processes, how to obtain high quality perovskite films with high coverage, desired crystal morphology, excellent crystallinity and fewer defects is regarded as one of the pivotal factors for high performance PSCs.[8–11] Perovskite films prepared by solution processes are usually composed of nanoscale grains so that there are a number of boundaries in the films. Ginger and co-workers reported that the photoluminescence intensity in grain boundaries was lower than that in grains along with a faster non-radiative decay.[12] Huang and co-workers also reported that ion migration at grain boundaries was faster than in grain interiors.[13] Therefore, the monolayer of the perovskite with a single crystal cross-sectional profile is considered to be the desired active layer for solar cells owing to the low trap density and high large charge carrier mobility.

To date, one-step spin-coating has been a typical solution process for the fabrication of perovskite films. However, inhomogeneous crystallization with removal of the solvent results in typical branch-like perovskite grains.[14,15] The anti-solvent method based on one-step spin-coating has become the most widely used method to produce the desired crystal morphology due to the fast nucleation process.[2,16] During spin-coating, excessive amounts of solvents, such as toluene,[17] chlorobenzene,[16] diethyl ether or ethyl acetate,[18,19] are dropped on the wet film to extract the solvent of the precursor and induce crystallization of the perovskite in a very short time. This generates a large number of crystal nuclei, which grow to form a compact perovskite film. However, fast precipitation from the top to the bottom of the perovskite film may cause inhomogeneous crystallization of perovskite crystals. Moreover, this method shows poor reproducibility due to the rigorous anti-solvent dropping time. Recently, intensive studies have been focused on retarding the crystallization process of the perovskite to develop high quality films.[9,17,20,21] For example, Lewis bases such as *N*,*N*-dimethyl sulfoxide (DMSO) have been employed as electron donors to form an intermediate phase to avoid the fast precipitation of plate-like PbI_2.[18] Such a method also yields nanoscale

[a]Institute of Advanced Materials and Technology, University of Science and Technology Beijing, 100083, China. E-mail: tianjianjun@mater.ustb.edu.cn
[b]Department of Physics, University of Miami, Coral Gables, 33146, USA
[c]Department of Materials and Engineering, University of Washington, Seattle, WA 98195-2120, USA

† Electronic supplementary information (ESI) available. See DOI: 10.1039/c7ta08761f

perovskite grains with a large number of grain boundaries, which affect the charge carrier kinetics and accelerate ion migration.[9,13,22] Hence, how to prepare monolayer perovskite films with a single crystal cross-sectional profile is still a challenge for PSCs.

Understanding the formation mechanism of solid perovskite films from the precursor solution is one of the fundamental rules to construct high-quality perovskite films. Our previous study showed that the additive of CH_3NH_3Cl (MACl) in the perovskite precursor could slow down the perovskite crystallization rate *via* forming intermediate phases.[19] The much more stable complex intermediate phases gradually transform into the perovskite structure with sublimation of MACl during thermal annealing. Recently, several interesting studies revealed that the nature of the perovskite precursor was a colloidal precursor rather than a "true" solution.[23–25] Both the crystallinity and morphology of the perovskite film would be improved by increasing the aging time of the precursor solution. In our previous study,[26] we also demonstrated that there were stable coordination complexes in the perovskite precursor, which could assemble into perovskite crystals during the annealing process. This indicates that the solution-based one step spin-coating process for the fabrication of perovskite films is similar to the so-called sol–gel method.[27] The sol precursor changes to the gel wet film with removal of solvent.[28–30] However, few studies have focused on the effect of colloidal characteristics on the formation of perovskite films. We deem that high-quality perovskite films can be obtained by designing and controlling the colloidal characteristics of the perovskite precursor.

Herein, we report colloidal cluster engineering based on coordination interactions to fabricate compact perovskite films with a single crystal cross-sectional profile. Stable and large size colloidal clusters of coordination complexes in the standard $CH_3NH_3PI_3$ ($MAPbI_3$) precursor solution are formed by introducing both DMSO and MACl. The large clusters are spin-coated on the substrate to induce intermediate phase monolayer films, which transform into large perovskite grains during the annealing process. The produced monolayer perovskite films exhibit compact micron-scale grains with enhanced crystallinity and reduced trap-state density. As a result, the solar cell based on the monolayer film shows a high PCE of 19.14%, which is much higher than that of the devices based on the regular multilayer film (15.12%).

Experimental section

Materials synthesis and solution preparation

CH_3NH_3I (MAI) and CH_3NH_3Cl (MACl) were synthesized by the reported methods.[31,32] The synthesized 200 mg MAI powder and 576 mg PbI_2 (Yingkou You Xuan Trade Co., Ltd) were sequentially dissolved in 1 mL *N*,*N*-dimethylformamide (DMF, 99.8%, Sigma-Aldrich) to form the standard perovskite precursor solution. The precursor solution was filtered using a 0.44 μm pore PVDF syringe filter, and then stoichiometric ratios of DMSO, MACl and DMSO + MACl were added to the standard perovskite precursors to prepare colloidal engineering perovskite precursors. Unless otherwise noted, the molar ratio of MAI : PbI_2 : DMSO was 1 : 1 : 1.

$MAI{\cdot}PbI_2{\cdot}MACl{\cdot}DMF$ and $MAI{\cdot}PbI_2{\cdot}DMSO{\cdot}MACl{\cdot}DMF$ solid complexes were obtained by adding 3 mL ethyl acetate (EA) to 1 mL MACl and DMSO + MACl mixture precursors, respectively. The produced solid complexes were further filtered and dried at 60 °C in a vacuum oven for 3 h.

The compact TiO_2 precursor solution was prepared by diluting titanium diisopropoxide bis(acetylacetonate) (75 wt% in isopropanol) in ethanol with a volume ratio of 1 : 25. Mesoporous TiO_2 paste was prepared by diluting commercial TiO_2 nanoparticle paste (Dyesol 18NRT, Dyesol) in ethanol with a weight ratio of 1 : 14. The hole-transporting layer precursor solution was prepared by dissolving 72.3 mg Spiro-MeOTAD in 1 mL chlorobenzene. To this solution, 29 μL 4-*tert*-butylpyridine and 17.5 μL lithium bis(trifluoromethanesulfonyl)imide salt solution in acetonitrile (520 mg mL^{-1}) were added, respectively.

Materials synthesis and solution preparation

The etched FTO glasses were cleaned in an ultrasonic bath using deionized water, acetone and ethanol for 15 min, respectively, and then under UV ozone treatment for 15 min before spray pyrolysis deposition. A 30 nm compact TiO_2 layer was coated by spray pyrolysis deposition at 450 °C, followed by annealing for 30 min. An ultrathin mesoporous TiO_2 layer was deposited on the compact TiO_2 by spin-coating at 5000 rpm for 30 s, and then annealed at 500 °C for 30 min. 40 μL colloidal perovskite precursor solution was spin-coated on the mesoporous TiO_2 layer at 3000 rpm for 40 s, and 200 μL of anti-solvent EA was dropped on the center of the substrate in 6–24 s to induce a perovskite intermediate phase. Then the wet film was annealed at 100 °C for 90 min on a hotplate. When the substrate was cooled down, 25 μL spiro-MeOTAD solution was spin-coated on the perovskite film at 4000 rpm for 30 s. After oxidation for 12 h in a desiccator, a 50 nm Ag electrode was deposited onto the substrate through a shadow mask by thermal evaporation with the base pressure of $<5 \times 10^{-5}$ Pa. The active area of the device is 0.1 cm^2.

Characterization

Dynamic light scattering (DLS) measurements were performed using a 90Plus PALS (Brookhaven Instruments Corporation), and the concentration of perovskite precursors was 0.25 M. Fourier transform infrared spectroscopy (FTIR) was performed using a Bruker Vertex 80v spectrometer, and the concentration of perovskite precursors was 1 M. Scanning electron microscopy (SEM) measurements were performed using a cold field emission scanning electron microscope (SU8020, Hitachi). Atomic force microscopy (AFM) images were obtained using an MFP-3D Infinity AFM (Asylum Research, Oxford Instruments). The XRD patterns were obtained using an X-ray diffractometer (PANalytical, Netherlands) with a monochromatic Cu Kα radiation source ($\lambda = 1.54056$ Å). *In situ* XRD measurements were performed in a vacuum chamber at 100 °C. The absorption spectra were recorded using an ultraviolet-visible (UV-vis) spectrophotometer (UV-3600, Shimadzu). The photoluminescence (PL)

spectra were measured using a steady state fluorescence spectrometer (FLS980, Edinburgh), and the excitation wavelength was 375 nm. The current–voltage characteristics were recorded using a digital source meter (2400, Keithley Instruments Inc.) under 3 A grade AM 1.5 G simulated sunlight (100 mW cm^{-2}) (7-SS1503A, 7 Star Optical Instruments Co., Beijing, China). The incident light intensity was calibrated with an NREL-calibrated Si solar cell (Newport, Stratford Inc., 91150V). The incident photon conversion efficiency (IPCE) was measured in the direct current (DC) mode using a custom measurement system consisting of a 150 W xenon lamp (7ILX150A, 7 Star Optical Instruments Co., Beijing, China), a monochromator (7ISW30, 7 Star Optical Instruments Co., Beijing, China) and a digital source meter (2400, Keithley Instruments Inc.).

Results and discussion

As shown in Fig. S1,† the Tyndall effect of the colloidal characteristic was observed obviously for the perovskite precursors under red light illumination in the dark, indicating that the precursors are colloidal dispersions rather than "true" solutions. This result has also been confirmed by previous studies.[23,25] For the colloidal solution, there are a number of colloidal clusters that are dispersed in the solvent.[28] Fig. 1(a) shows the schematic illustration of the formation of perovskite films from the colloidal perovskite precursors to solid thin films. During the spin-coating process, the sol precursors transform into gel wet films with removal of solvent. When the size of colloidal clusters is much less than the thickness of the wet film, the multilayer gel wet film is formed by close packing of small crystal grains. On the contrary, the large size clusters can be orderly arranged on the substrate with removal of solvent to produce a monolayer gel wet film. Then the intermediate phases of wet films transform into the perovskite structure during annealing. Hence, we propose a colloidal cluster strategy to obtain the desired perovskite film by controlling the colloidal cluster size of the perovskite precursor solution using the additive of MACl. In addition, DMSO is employed to stabilize the colloidal characteristics of colloidal clusters.

Dynamic light scattering (DLS) was employed to detect the size distributions of the colloidal clusters in the perovskite precursor solutions. Fig. 1(b) shows the statistical size distributions of the perovskite precursor according to DLS spectra. In the case of the standard perovskite precursor, the average size of

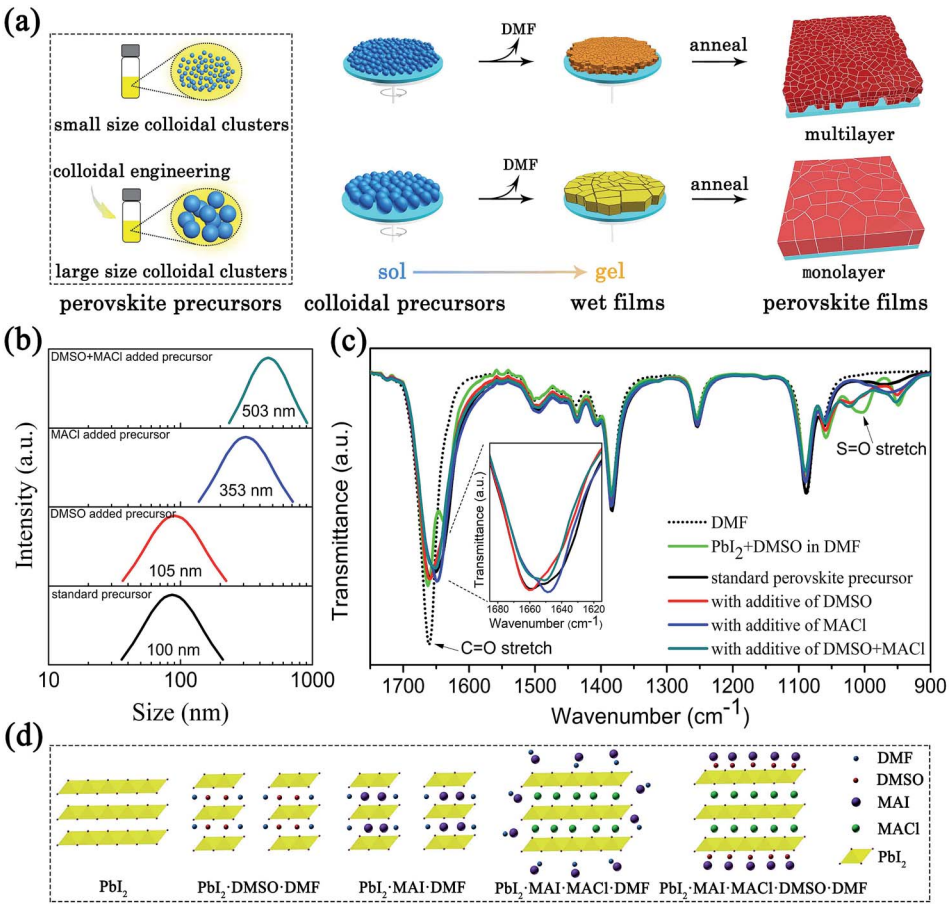

Fig. 1 (a) Schematic illustrations of the formation of perovskite films from precursors to final perovskite films; (b) size distributions of different colloidal perovskite precursors measured by DLS spectra; (c) FTIR spectra of different colloidal perovskite precursors (inset: FTIR spectra of different colloidal perovskite precursors in the range of 1685–1615 cm^{-1}); (d) schematic of the structures of colloidal clusters in different colloidal precursors.

the colloidal clusters is around 100 nm, while the average size of colloidal clusters for the perovskite precursor with the additive of DMSO is also around 105 nm. This demonstrates that DMSO has little effect on the size of the colloidal clusters. For the perovskite precursor with the additive of MACl, the average size of colloidal clusters is up to 353 nm. The average size of the colloidal clusters further increases to 503 nm with the introduction of both DMSO and MACl. Fig. S2† shows the surface scanning electron microscopy (SEM) images of produced perovskite films prepared from the different perovskite precursors (the concentration of perovskite precursors was 0.25 M). It can be seen that the average grain size of produced perovskite films is 120 nm, 110 nm, 900 nm and 1 μm for the standard perovskite precursor and with the additives of DMSO, MACl and DMSO + MACl, respectively. For the perovskite precursor without the additive of MACl, the results are well consistent with the average size of colloidal clusters as shown in Fig. 1(b), while the average sizes of perovskite grains prepared using MACl and DMSO + MACl additives are much larger than that of colloidal clusters. The main reason is that the introduction of Cl^- into the perovskite precursor may reduce the activation energy of grain boundary migration to further enlarge the perovskite grain size during thermal annealing.[33–35] So the size of colloidal clusters in the perovskite precursor shows a strong correlation with the grain size of produced perovskite crystals. It is well known that PbI_2 is a 2-dimensional (2D) layered material, held together by van der Waals interactions with an interlayer spacing of ~2.6 Å.[36] When the guest molecules (such as DMF, DMSO and MAI) are introduced into the precursor solution, the layered PbI_2 framework undergoes intercalation with the guest molecules to form coordination complexes.[17,37,38] To delineate the formation of the coordination complexes, Fourier transform infrared (FTIR) spectroscopy was carried out to reveal the coordination interaction. Our previous study showed that the stretching vibration of the C=O bond appeared at 1660 cm^{-1} for pure DMF, while it shifted to 1633 cm^{-1} upon interaction with PbI_2.[26] As shown in Fig. 1(c), in the case of the standard perovskite precursor, the vibration peak for the $PbI_2 \cdot DMF$ complex at 1633 cm^{-1} is not observed, while the vibration peak with a broad full width half maximum (FWHM) at 1660 cm^{-1} could be ascribed to the C=O bond of pure DMF. This demonstrates that the affinity of MAI toward PbI_2 is higher than that of DMF toward PbI_2, so the colloidal clusters of $PbI_2 \cdot MAI \cdot DMF$ complexes are formed by the substitution of MAI for DMF. It is worth mentioning that a small shoulder at 1650 cm^{-1} is also observed, which is well consistent with the frequency of MAI in DMF solution as shown in Fig. S3.† Therefore, the interaction of MAI with DMF should be responsible for the small size of colloidal clusters for the standard perovskite precursor. As for the perovskite precursor with the additive of MACl, the vibration peak of C=O shifts from 1660 cm^{-1} to 1648 cm^{-1}, which is close to that of MAI in DMF solution as discussed above. As shown in Fig. S4,† although MACl cannot be dissolved in pure DMF, it can be easily dissolved in the standard perovskite precursor at room temperature. Hence, the strong interaction of MACl with PbI_2 may induce the formation of the stable complex $PbI_2 \cdot MACl_x \cdot MAI_{1-x} + (x)MAI \cdot DMF$ by the substitution of MACl for MAI, which can increase the size of colloidal clusters. Compared to the perovskite precursors with the additive of MACl or DMSO, both vibration peaks of C=O and S=O shift slightly for the perovskite precursor with additives of DMSO + MACl, indicating the interaction of DMSO with the colloidal clusters. Fig. 1(d) shows the schematic of the structures of the coordination complexes in different colloidal precursors. The layered PbI_2 would act as the framework of the coordination complexes *via* coordination interactions. In order to further verify the coordination interaction of colloidal clusters in the perovskite precursor, ethyl acetate (EA) was employed as an extraction agent to obtain the gel coordination complex. In our previous study, due to the weak interaction between MAI and PbI_2, the obtained complex divided into the white upper layer (MAI) and yellow bottom layer (PbI_2) from the standard perovskite precursor.[26] As shown in Fig. S5(a),† for the perovskite precursor with the additive of MACl, the gel complex was obtained, while it changed to a solid precipitate and lost its fluidity after shaking a few times. However, for the perovskite precursor with additives of DMSO and MACl, the gel complex showed excellent stability, and the gel characteristic of the complex was retained after shaking. This suggests that DMSO can stabilize the colloidal characteristics of the colloidal clusters. Fig. S5(b)† shows the *in situ* X-ray diffraction (XRD) patterns of the complex before and after annealing. The presence of XRD patterns at low angles indicates the intercalation of the solvent molecules into the PbI_2 structure. The formation of the solvates for the complexes is also confirmed by the FTIR spectra as shown in Fig. S5(c).† After annealing for 3 min, the complex from the precursor with additives of DMSO + MACl exhibits better crystallinity than the complex from the precursor with only MACl. Further increasing the annealing time to 30 min, both the complexes convert to a $MAPbI_3$ tetragonal phase. The intensity of the (110) plane for the perovskite from the precursor with additives of DMSO + MACl is 13-fold that of the perovskite from the precursor with only MACl. This demonstrates that the stability of the colloidal clusters is correlated with the crystallinity of the final perovskite crystals.

Fig. 2(a) and (b) show the surface SEM images of the perovskite films prepared from the standard perovskite precursors and with additives of DMSO + MACl, respectively. It is worth mentioning that the optimized concentration of perovskite precursors is 1.25 M with a stoichiometric ratio of 1 : 1 : 1 : 0.6 for MAI : PbI_2 : DMSO : MACl, which is the same condition used for device fabrication. The average grain size of the perovskite film prepared from the standard precursor is around 230 nm, which is in accordance with the literature.[16,18] For the perovskite precursor with additives of DMSO + MACl, the average size of perovskite grains is around 3 μm, which is an order of magnitude larger than that of the control sample. Fig. S6(a)–(d)† show the topography and three-dimensional atomic force microscopy (AFM) images of the perovskite films prepared from the standard perovskite precursors and with additives of DMSO + MACl. The apparent grain size observed in the AFM images is consistent with that of SEM images shown in Fig. 2(a) and (b), and the root mean square roughness values are

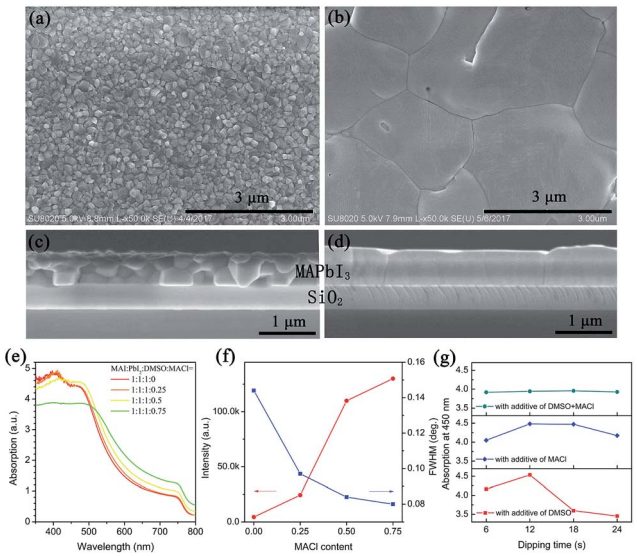

Fig. 2 Surface SEM images of the perovskite films prepared using the precursors with additives of DMSO (a), and DMSO + MACl (b). Cross-sectional SEM images of perovskite films prepared using the precursors with additives of DMSO (c), and DMSO + MACl (d). UV-vis absorption spectra (e) of perovskite films prepared from the different amounts of MACl in the DMSO + MACl mixture perovskite precursor. (f) XRD diffraction intensity and FWHM of the (110) plane as a function of MACl content. (g) The absorption at 450 nm as a function of anti-solvent dropping time for the perovskite films prepared using the different colloidal perovskite precursors.

14.8 and 31.9 nm (5 μm × 5 μm in size), respectively. Fig. S7† shows the surface SEM images of the perovskite films prepared from the DMSO + MACl perovskite precursor with different amounts of MACl, and the average grain size is ~0.24 μm for 0 M MACl, ~0.75 μm for 0.25 M MACl, ~2.5 μm for 0.5 M MACl and ~3.5 μm for 0.75 M MACl. Fig. 2(c) and (d) show the cross-sectional SEM images of the perovskite films prepared from the standard perovskite precursors and with additives of DMSO + MACl. In order to minimize the impact of substrates (for example roughness), we chose the SiO_2/Si substrates. It is clearly shown that the former film is multilayered, which is formed by close packing of small perovskite grains. There are many grain boundaries along the cross-section of the film. The latter film is monolayered, and the size of grains is equal to the thickness of the film along the cross-section of the film. In addition, the grain boundaries are vertical, which would reduce the resistance of charge carrier transport.[39,40] Fig. S8(a) and (b)† show the cross-sectional SEM images of multilayer and monolayer perovskite films on FTO substrates. In the case of the multilayer film, although the surface coverage is nearly 100%, there are many voids at the interface of FTO/perovskite, which may be induced by the fast precipitation of the anti-solvent method from top to bottom. The morphology of the monolayer perovskite on the FTO substrate is similar to that on the SiO_2 substrate. Fig. 2(e) shows the effect of MACl content on the UV-vis absorption spectra of perovskite films prepared from the colloidal precursors with additives of MACl + DMSO. The absorption increases with the amount of MACl from 0.25 M to 0.5 M. When the amount of MACl increases to 0.75 M, the absorption in the short wavelength region decreases due to the voids in the perovskite film, which is consistent with SEM images shown in Fig. S7(h).† The increase of absorption in the long-wavelength region is attributed to light scattering.[41] Fig. 2(f) shows the XRD diffraction peak intensity and FWHM of the (110) plane as a function of MACl content (the XRD patterns are shown in Fig. S9†). It is clearly shown that the produced films exhibit enhanced crystallization with increasing the amount of MACl. We also investigate the reproducibility of the anti-solvent method by using UV-vis absorption spectra. Fig. 2(g) shows the absorption value at 450 nm as a function of anti-solvent dropping time, and the UV-vis absorption spectra are shown in Fig. S10.† For the films from the perovskite precursors with only one additive of DMSO or MACl, the absorption value changes obviously with the anti-solvent dropping time. The optimum anti-solvent dropping time is usually very short (within a few seconds), which is not beneficial to the reproducibility of the fabrication. For the perovskite films prepared from the precursor with additives of DMSO + MACl, the absorption at 450 nm is nearly constant with increasing the anti-solvent dropping time from 6 s to 24 s, indicating that the introduction of DMSO + MACl could significantly improve the reproducibility of the anti-solvent method.

XRD was employed to track the crystallization evolution of the perovskite from the gel wet film (before annealing) to the final perovskite film (after annealing). Fig. 3(a) shows the XRD patterns of the wet films prepared from the different colloidal perovskite precursors. For the wet films prepared from the standard perovskite precursor, the low intensity of XRD diffraction peaks at small angles (6.60° and 9.57°) is attributed to the solvate intermediate phase, while the main diffraction peaks of the $MAPbI_3$ tetragonal phase at 14.16° and 28.48° are clearly identified due to the weak interaction between DMF and PbI_2. In the presence of equimolar DMSO in the perovskite precursor, the XRD diffraction peaks of the solvate intermediate phase at small angles (7.12° and 9.23°) are detected. The absence of the $MAPbI_3$ phase indicates that perovskite crystallization is retarded due to the strong interaction between DMSO and PbI_2. These results are well consistent with the previous literature.[14,17] In the case of the perovskite precursor with the additive of MACl, the characteristic diffraction peaks of the $MAPbCl_3$ cubic phase at 15.63° and 31.51°are observed for the wet film, respectively. The absence of small angle diffraction peaks of the solvate intermediate phase indicates the strong interaction between MACl and PbI_2, which is consistent with the FTIR results as discussed above. For the perovskite precursor with additives of DMSO + MACl, the enhanced intensity of the solvate intermediate phase at 9.25° indicates the formation of the ordered intermediate phase. As shown in Fig. 3(b), the solvate intermediate phases convert to the $MAPbI_3$ tetragonal phase immediately after drying treatment for both the wet films prepared from the standard perovskite precursor and with the additive of DMSO. However, the characteristic peaks of the $MAPbCl_3$ cubic phase at 15.68° and 31.60° are observed in the dry film with additives of DMSO and MACl, which exhibits a strong preferential orientation along the (100)

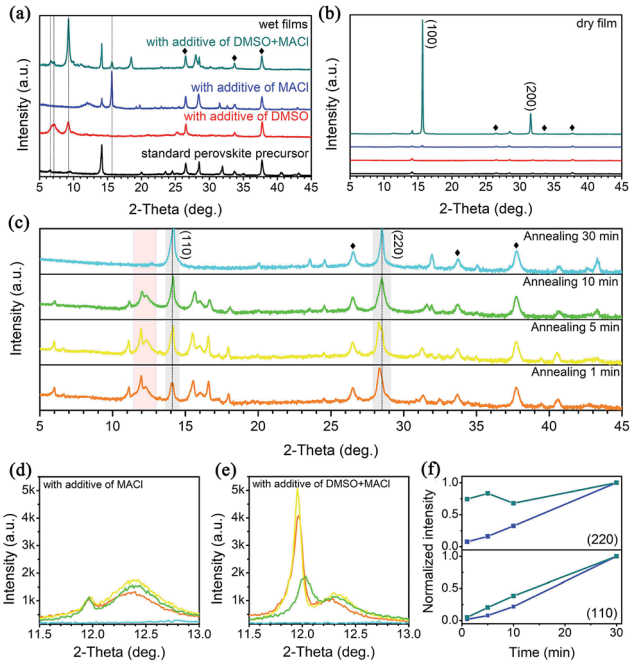

Fig. 3 XRD patterns of wet films (a) and dry treatment films (b) which were prepared from different perovskite precursors; XRD patterns (c) of crystallization evolution as a function of annealing time on a logarithmic scale for perovskite films prepared from the perovskite precursor with additives of DMSO + MACl; the selected XRD patterns of perovskite films prepared from the perovskite precursor with the additives of MACl (d) and DMSO + MACl (e) at different annealing times, which exhibit characteristic diffraction peaks at 11.5–13°. The normalized intensity (f) of the (110) and (220) planes of $MAPbI_3$ prepared from the perovskite precursor with additives of MACl (blue) and DMSO + MACl (dark cyan) as a function of annealing time.

and (200) crystal planes. The formation of the high crystallinity $MAPbCl_3$ phase in the drying stage is mainly attributed to the stable colloidal clusters with the ordered structure. Fig. 3(c) shows the XRD patterns of perovskite films with the additives of DMSO + MACl at different thermal annealing durations. The $MAPbCl_3$ cubic phase is converted to the metastable intermediate phases at 5.99°, 11.11°, 11.97°and 12.28° within 1 min. Besides, a strong diffraction peak at 28.31° is also observed, which corresponds to the (220) plane of the $MAPbI_3$ phase with an enlarged interplanar spacing. Fig. 3(d) and (e) show the intermediate phase crystallization evolution as a function of annealing time for perovskite films with additives of MACl and DMSO + MACl, respectively (the XRD patterns of perovskite films with the additive of MACl with different annealing durations are shown in Fig. S11†). After annealing for 5 min, for the perovskite film with the additive of MACl, the main diffraction peak of intermediate phases around 12.4° is associated with the (001) plane of the PbI_2 phase with an enlarged interplanar spacing,[19,42] while enhanced intensity of the diffraction peak at 11.97° is detected for the perovskite film with the additives of DMSO + MACl. Although the origin of the diffraction peak at 11.97° is still not clear, the enhanced degree of the long-range order of the intermediate phase changes the perovskite crystallization kinetics, which is correlated with the structure of colloidal clusters. On further prolonging the annealing time, the intensity of diffraction peaks around 11.97° and 12.29°decreases gradually. Fig. 3(f) shows the normalized intensity of the (110) and (220) planes of $MAPbI_3$ with additives of MACl and DMSO + MACl at different annealing durations, respectively. The intensity of the (110) plane of the perovskite structure increases with increasing annealing time. However, the intensity of the (220) plane for the sample from the perovskite precursor with additives of DMSO + MACl changes little during the annealing process. This implies that the formation of the perovskite phase may be the "direct formation mechanism". Such a mechanism has been reported by Chang and coworkers, which can improve the quality of perovskite crystals.[43]

The photovoltaic characteristics of the resulting perovskite films are further examined. The configuration of the device is FTO/compact TiO_2/ultrathin mesoporous TiO_2/$MAPbI_3$/spiro-OMeTAD/Ag. In this study, the optimum stoichiometric ratio of MAI : PbI_2 : DMSO : MACl is 1 : 1 : 1 : 0.6 for the colloidal engineering perovskite precursor. Fig. 4(a) shows the *J–V* curves of the PSCs assembled using conventional multilayer and monolayer perovskite films, respectively. As for the multilayer perovskite film based solar cell, the PCE is 15.12% with a short-circuit current density (J_{sc}) of 18.88 mA cm^{-2}, open-circuit voltage (V_{oc}) of 1.06 V and fill factor (FF) of 75.53%. It is worth noting that in the case of multilayer perovskite film solar cells, the Ag electrode of the device becomes invisible under 1 sun illumination (from the glass side) and the photographs of devices are shown in Fig. S12.† As discussed above, the voids at the interface of FTO/perovskite for the multilayer perovskite film not only reduce light absorption, but also influence change transportation, which should be responsible for the relatively

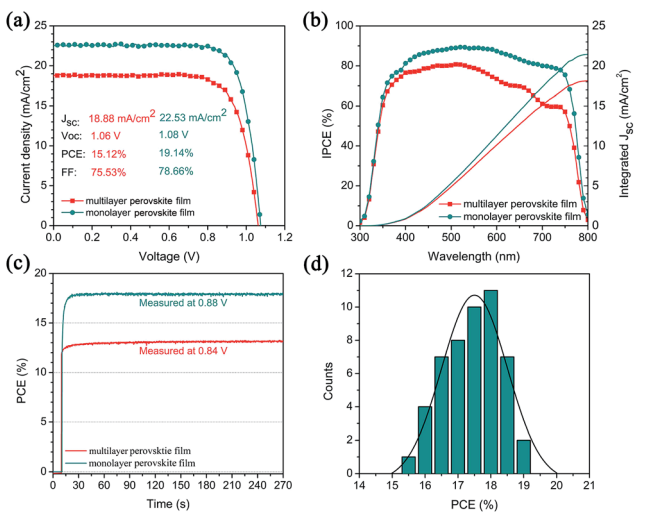

Fig. 4 The *J–V* curves (a) and IPCE (b) of PSCs assembled using the different perovskite films. The multilayer perovskite films were prepared using the perovskite precursor with a stoichiometric ratio of MAI : PbI_2 : DMSO : MACl = 1 : 1 : 1 : 0; the monolayer perovskite film was prepared using the perovskite precursor with a stoichiometric ratio of MAI : PbI_2 : DMSO : MACl = 1 : 1 : 1 : 0.6. (c) The stabilized PCE is measured at the maximum power point of PSCs. (d) PCE statistical distribution of monolayer perovskite film based PSCs (50 devices).

low J_{sc}. The PSCs assembled using the monolayer perovskite film show a high J_{sc} of 22.53 mA cm^{-2} due to the better charge transportation of the monolayer perovskite film. A high V_{oc} of 1.08 V is obtained, which yields a PCE of 19.14%. The impressive FF reaches 78.66% due to the reduced series resistance from 30.9 Ω to 13.6 Ω that was calculated from the *J*–*V* curves. Fig. 4(b) shows the incident photon-to-electron conversion efficiency (IPCE) spectra and the integrated J_{sc} for PSCs based on the different films. The IPCE of the monolayer perovskite film based solar cell surpasses 80% in the region of 397–702 nm, while that of the multilayer perovskite film based solar cell is close to 80% in a narrow region of 467–532 nm. The integrated J_{sc} of the two devices is 21.5 mA/cm^2 and 18.1 mA cm^{-2}, respectively, consistent with the J_{sc} obtained from *J*–*V* curves. Fig. 4(c) shows the stabilized PCE that was measured at the maximum power point, and the monolayer perovskite film based device shows a stabilized PCE of 17.9%. As a comparison, the multilayer perovskite film based solar cell shows a stabilized PCE of 13.1%. We also compared the hysteresis of PCEs prepared from perovskite precursors with different amounts of MACl. Fig. S13† shows the typical hysteresis of the forward scanning and reverse scanning of *J*–*V* curves, the forward scanning PCE corresponds to 78.3% and 85.6% of their reverse scanning PCE for MAI : PbI_2 : DMSO : MACl = 1 : 1 : 1 : 0.3 and 1 : 1 : 1 : 0.6 colloidal perovskite precursors, respectively. According to the literature,[44] the hysteresis index is 0.22 and 0.14, respectively. The difference is close to the reported results based on high-quality perovskite films.[35,44,45] Fig. 4(d) shows the reproducibility of the monolayer perovskite film based PSCs, and the average PCE reaches 17.5%, which is mainly attributed to the excellent reproducibility of perovskite films as mentioned above.

The ideality factor n under illumination was defined according to the equation $n = \frac{q}{kT}\frac{dV_{oc}}{d\ \ln(\varphi)}$, which was commonly used to reveal the recombination mechanism of devices.[46,47] Fig. 5(a) shows the dependence of V_{oc} on the light intensity of PSCs assembled using the monolayer and monolayer perovskite films, respectively. Both PSCs show comparable V_{oc} values under 1 sun light intensity. However, the V_{oc} of the multilayer perovskite film based solar cell drops fast with the decrease of light intensity. The assessed ideality factor n is equal to 1.45, in the presence of both trap-assisted and bimolecular recombination.[47–49] For the monolayer perovskite film based solar cell, the ideality factor n decreases to 1.14, indicating that the trap-assisted recombination is suppressed due to the enhanced crystallinity and reduced recombination centers in the monolayer perovskite film.[9] Fig. 5(b) shows the steady-state PL spectra of the perovskite films. Both the perovskite emission peaks show typical Stokes shifts around 770 nm, which is consistent with the literature,[50] while the FWHM is slightly narrowed for the monolayer perovskite film, indicating that the charge recombination is reduced due to the enhanced crystallinity. We also fabricated FTO/compact TiO_2/$MAPbI_3$/PCBM/Ag devices to further assess the trap-state density in perovskite films by using the space-charge-limited-current (SCLC). Fig. 5(c) and (d) show *J*–*V* curves on a logarithmic scale. The current

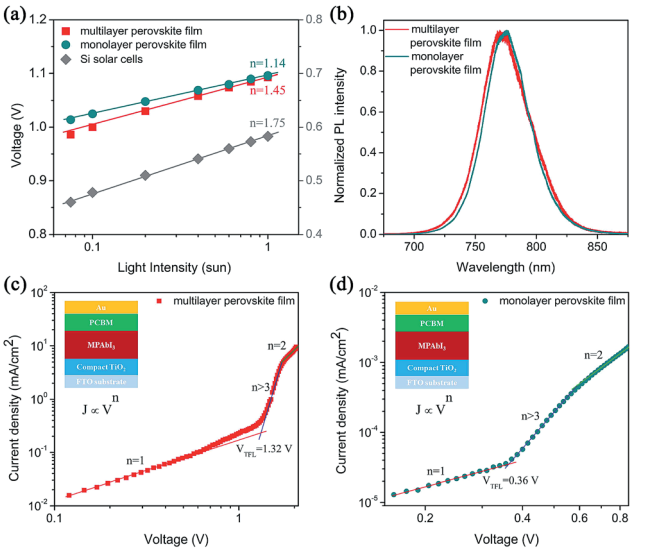

Fig. 5 Voltage dependence of light intensity (a) of multilayer perovskite film and monolayer perovskite film PSCs. The steady-state PL spectra (b) of perovskite films prepared from multilayer and monolayer perovskite films on the SiO_2 substrate. Space-charge-limited-current of FTO/compact TiO_2/$MAPbI_3$/PCBM/Ag devices with the multilayer perovskite film (c) and monolayer perovskite film (d).

density exhibits a linear rise in the ohmic regime, and the nonlinear regimes correlate with a trap-filled limit and space charge limited current according to $n(J \propto V^n)$.[51,52] The trap-state density can be determined by the equation $n_{trap} = \frac{2\varepsilon_0\varepsilon\ V_{TFL}}{eL^2}$. We estimated the trap-state density n_{trap} to be 2.9 × 10^{16} cm^{-3} and 6.8 × 10^{15} cm^{-3} for the multilayer and monolayer perovskite film based solar cells, respectively. This indicates that the trap-states in the monolayer perovskite film are effectively reduced, and hence the device performance can be improved.

Conclusions

A colloidal engineering strategy by controlling the size of colloidal clusters in the perovskite precursor was developed to induce monolayer perovskite films. The introduction of MACl into the standard perovskite precursor significantly increased the size of colloidal clusters, meanwhile, DMSO was further employed to stabilize the characteristics of the colloidal clusters and improve the reproducibility of the anti-solvent method. The coordination complexes composed of stable and large size colloidal clusters were confirmed in the colloidal engineering perovskite precursor solution. During the spin-coating process, the formed large size colloidal clusters were orderly arranged on the substrate to form monolayer wet films (intermediate phase). Then the large clusters transformed into perovskite crystals, which grew to form large grains with an average size of 3 μm after annealing. Due to the much lower trap state density and higher crystallinity of the monolayer perovskite films, a power conversion efficiency (PCE) of 19.14% was achieved. Therefore, this study sheds light on the conversion mechanism of perovskite crystals from colloidal precursors to solid films, and paves

the way for further improvement of high-quality perovskite films that can lead to high performance devices.

Conflicts of interest

There are no conflicts to declare.

Acknowledgements

This work was supported by the National Science Foundation of China (51774034, 51772026, and 51611130063), Fundamental Research Funds for the Central Universities (FRF-BD-16-012A) and the 111 Project (No. B17003).

References

1 A. Kojima, K. Teshima, Y. Shirai and T. Miyasaka, Organometal Halide Perovskites as Visible-Light Sensitizers for Photovoltaic Cells, *J. Am. Chem. Soc.*, 2009, **131**, 6050–6051.

2 D.-Y. Son, J.-W. Lee, Y. J. Choi, I.-H. Jang, S. Lee, P. J. Yoo, H. Shin, N. Ahn, M. Choi, D. Kim and N.-G. Park, Self-formed grain boundary healing layer for highly efficient $CH_3NH_3PbI_3$ perovskite solar cells, *Nat. Energy*, 2016, **1**, 16081.

3 H. S. Kim, C. R. Lee, J. H. Im, K. B. Lee, T. Moehl, A. Marchioro, S. J. Moon, R. Humphry-Baker, J. H. Yum, J. E. Moser, M. Gratzel and N. G. Park, Lead iodide perovskite sensitized all- solid-state submicron thin film mesoscopic solar cell with efficiency exceeding 9%, *Sci. Rep.*, 2012, **2**, 591.

4 J. Huang, Y. Yuan, Y. Shao and Y. Yan, Understanding the physical properties of hybrid perovskites for photovoltaic applications, *Nat. Rev. Mater.*, 2017, **2**, 17042.

5 K. X. Steirer, P. Schulz, G. Teeter, V. Stevanovic, M. Yang, K. Zhu and J. J. Berry, Defect Tolerance in Methylammonium Lead Triiodide Perovskite, *ACS Energy Lett.*, 2016, **1**, 360–366.

6 M. J. Carnie, C. Charbonneau, M. L. Davies, J. Troughton, T. M. Watson, K. Wojciechowski, H. Snaith and D. A. Worsley, A one-step low temperature processing route for organolead halide perovskite solar cells, *Chem. Commun.*, 2013, **49**, 7893–7895.

7 J. Burschka, N. Pellet, S. J. Moon, R. Humphry-Baker, P. Gao, M. K. Nazeeruddin and M. Gratzel, Sequential deposition as a route to high-performance perovskite-sensitized solar cells, *Nature*, 2013, **499**, 316–319.

8 B. Li, J. Tian, L. Guo, C. Fei, T. Shen, X. Qu and G. Cao, Dynamic Growth of Pinhole-Free Conformal $CH_3NH_3PbI_3$ Film for Perovskite Solar Cells, *ACS Appl. Mater. Interfaces*, 2016, **8**, 4684–4690.

9 C. Fei, B. Li, R. Zhang, H. Fu, J. Tian and G. Cao, Highly Efficient and Stable Perovskite Solar Cells Based on Monolithically Grained $CH_3NH_3PbI_3$ Film, *Adv. Energy Mater.*, 2016, 1602017.

10 W. Li, J. Fan, J. Li, Y. Mai and L. Wang, Controllable Grain Morphology of Perovskite Absorber Film by Molecular Self-Assembly toward Efficient Solar Cell Exceeding 17, *J. Am. Chem. Soc.*, 2015, **137**, 10399–10405.

11 Z. Xiao, Q. Dong, C. Bi, Y. Shao, Y. Yuan and J. Huang, Solvent annealing of perovskite-induced crystal growth for photovoltaic-device efficiency enhancement, *Adv. Mater.*, 2014, **26**, 6503–6509.

12 D. W. deQuilettes, S. M. Vorpahl, S. D. Stranks, H. Nagaoka, G. E. Eperon, M. E. Ziffer, H. J. Snaith and D. S. Ginger, Solar cells. Impact of microstructure on local carrier lifetime in perovskite solar cells, *Science*, 2015, **348**, 683–686.

13 Y. Shao, Y. Fang, T. Li, Q. Wang, Q. Dong, Y. Deng, Y. Yuan, H. Wei, M. Wang, A. Gruverman, J. Shield and J. Huang, Grain boundary dominated ion migration in polycrystalline organic–inorganic halide perovskite films, *Energy Environ. Sci.*, 2016, **9**, 1752–1759.

14 S. Bae, S. J. Han, T. J. Shin and W. H. Jo, Two different mechanisms of $CH_3NH_3PbI_3$ film formation in one-step deposition and its effect on photovoltaic properties of OPV-type perovskite solar cells, *J. Mater. Chem. A*, 2015, **3**, 23964–23972.

15 A. R. Pascoe, Q. Gu, M. U. Rothmann, W. Li, Y. Zhang, A. D. Scully, X. Lin, L. Spiccia, U. Bach and Y.-B. Cheng, Directing nucleation and growth kinetics in solution-processed hybrid perovskite thin-films, *Sci. China Mater.*, 2017, **60**, 617–628.

16 M. Xiao, F. Huang, W. Huang, Y. Dkhissi, Y. Zhu, J. Etheridge, A. Gray-Weale, U. Bach, Y. B. Cheng and L. Spiccia, A fast deposition-crystallization procedure for highly efficient lead iodide perovskite thin-film solar cells, *Angew. Chem., Int. Ed.*, 2014, **53**, 10056–10061.

17 N. J. Jeon, J. H. Noh, Y. C. Kim, W. S. Yang, S. Ryu and S. I. Seok, Solvent engineering for high-performance inorganic-organic hybrid perovskite solar cells, *Nat. Mater.*, 2014, **13**, 897–903.

18 N. Ahn, D. Y. Son, I. H. Jang, S. M. Kang, M. Choi and N. G. Park, Highly Reproducible Perovskite Solar Cells with Average Efficiency of 18.3% and Best Efficiency of 19.7% Fabricated *via* Lewis Base Adduct of Lead(II) Iodide, *J. Am. Chem. Soc.*, 2015, **137**, 8696–8699.

19 C. Fei, L. Guo, B. Li, R. Zhang, H. Fu, J. Tian and G. Cao, Controlled growth of textured perovskite films towards high performance solar cells, *Nano Energy*, 2016, **27**, 17–26.

20 Y. Wu, A. Islam, X. Yang, C. Qin, J. Liu, K. Zhang, W. Peng and L. Han, Retarding the crystallization of PbI_2 for highly reproducible planar-structured perovskite solar cells via sequential deposition, *Energy Environ. Sci.*, 2014, **7**, 2934–2938.

21 L. Li, Y. Chen, Z. Liu, Q. Chen, X. Wang and H. Zhou, The Additive Coordination Effect on Hybrids Perovskite Crystallization and High-Performance Solar Cell, *Adv. Mater.*, 2016, **28**, 9862–9868.

22 J. S. Yun, J. Seidel, J. Kim, A. M. Soufiani, S. Huang, J. Lau, N. J. Jeon, S. I. Seok, M. A. Green and A. Ho-Baillie, Critical Role of Grain Boundaries for Ion Migration in Formamidinium and Methylammonium Lead Halide Perovskite Solar Cells, *Adv. Energy Mater.*, 2016, **6**, 1600330.

23 K. Yan, M. Long, T. Zhang, Z. Wei, H. Chen, S. Yang and J. Xu, Hybrid halide perovskite solar cell precursors: colloidal chemistry and coordination engineering behind device processing for high efficiency, *J. Am. Chem. Soc.*, 2015, **137**, 4460–4468.

24 H. Tsai, W. Nie, Y.-H. Lin, J. C. Blancon, S. Tretiak, J. Even, G. Gupta, P. M. Ajayan and A. D. Mohite, Effect of Precursor Solution Aging on the Crystallinity and Photovoltaic Performance of Perovskite Solar Cells, *Adv. Energy Mater.*, 2017, 1602159.

25 D. P. McMeekin, Z. Wang, W. Rehman, F. Pulvirenti, J. B. Patel, N. K. Noel, M. B. Johnston, S. R. Marder, L. M. Herz and H. J. Snaith, Crystallization Kinetics and Morphology Control of Formamidinium-Cesium Mixed-Cation Lead Mixed-Halide Perovskite via Tunability of the Colloidal Precursor Solution, *Adv. Mater.*, 2017, **29**, 1607039.

26 B. Li, C. Fei, K. Zheng, X. Qu, T. Pullerits, G. Cao and J. Tian, Constructing water-resistant $CH_3NH_3PbI_3$ perovskite films via coordination interaction, *J. Mater. Chem. A*, 2016, **4**, 17018–17024.

27 L. Spanhel and M. A. Anderson, Semiconductor clusters in the sol-gel process: quantized aggregation, gelation, and crystal growth in concentrated zinc oxide colloids, *J. Am. Chem. Soc.*, 1991, **113**, 2826–2833.

28 C. J. Brinker and G. W. Scherer., *Sol-gel science: the physics and chemistry of sol-gel processing*, Academic Press, 2013.

29 L. L. Hench and J. K. West, The sol-gel process, *Chem. Rev.*, 1990, **90**, 33–72.

30 L. Guo, C. Fei, R. Zhang, B. Li, T. Shen, J. Tian and G. Cao, Impact of sol aging on TiO_2 compact layer and photovoltaic performance of perovskite solar cell, *Sci. China Mater.*, 2016, **59**, 710–718.

31 J. H. Im, C. R. Lee, J. W. Lee, S. W. Park and N. G. Park, 6.5% efficient perovskite quantum-dot-sensitized solar cell, *Nanoscale*, 2011, **3**, 4088–4093.

32 Y. Zhao and K. Zhu, CH_3NH_3Cl-Assisted One-Step Solution Growth of $CH_3NH_3PbI_3$: Structure, Charge-Carrier Dynamics, and Photovoltaic Properties of Perovskite Solar Cells, *J. Phys. Chem. C*, 2014, **118**, 9412–9418.

33 S. Xiao, Y. Bai, X. Meng, T. Zhang, H. Chen, X. Zheng, C. Hu, Y. Qu and S. Yang, Unveiling a Key Intermediate in Solvent Vapor Postannealing to Enlarge Crystalline Domains of Organometal Halide Perovskite Films, *Adv. Funct. Mater.*, 2017, 1604944.

34 Y. Yang, S. Feng, M. Li, W. Xu, G. Yin, Z. Wang, B. Sun and X. Gao, Annealing Induced Re-crystallization in $CH_3NH_3PbI_{3-x}Cl_x$ for High Performance Perovskite Solar Cells, *Sci. Rep.*, 2017, **7**, 46724.

35 D. H. Kim, J. Park, Z. Li, M. Yang, J.-S. Park, I. J. Park, J. Y. Kim, J. J. Berry, G. Rumbles and K. Zhu, 300% Enhancement of Carrier Mobility in Uniaxial-Oriented Perovskite Films Formed by Topotactic-Oriented Attachment, *Adv. Mater.*, 2017, **29**, 1606831.

36 F. Hao, C. C. Stoumpos, Z. Liu, R. P. Chang and M. G. Kanatzidis, Controllable perovskite crystallization at a gas-solid interface for hole conductor-free solar cells with steady power conversion efficiency over 10%, *J. Am. Chem. Soc.*, 2014, **136**, 16411–16419.

37 W. S. Yang, J. H. Noh, N. J. Jeon, Y. C. Kim, S. Ryu, J. Seo and S. I. Seok, High-performance photovoltaic perovskite layers fabricated through intramolecular exchange, *Science*, 2015, **348**, 1234–1237.

38 Y. Jo, K. S. Oh, M. Kim, K.-H. Kim, H. Lee, C.-W. Lee and D. S. Kim, High Performance of Planar Perovskite Solar Cells Produced from PbI_2(DMSO) and PbI_2(NMP) Complexes by Intramolecular Exchange, *Adv. Mater. Interfaces*, 2016, **3**, 1500768.

39 C.-G. Wu, C.-H. Chiang, Z.-L. Tseng, M. K. Nazeeruddin, A. Hagfeldt and M. Grätzel, High efficiency stable inverted perovskite solar cells without current hysteresis, *Energy Environ. Sci.*, 2015, **8**, 2725–2733.

40 C.-H. Chiang, M. K. Nazeeruddin, M. Grätzel and C.-G. Wu, The synergistic effect of H_2O and DMF towards stable and 20% efficiency inverted perovskite solar cells, *Energy Environ. Sci.*, 2017, **10**, 808–817.

41 Y. Tian and I. G. Scheblykin, Artifacts in Absorption Measurements of Organometal Halide Perovskite Materials: What Are the Real Spectra, *J. Phys. Chem. Lett.*, 2015, **6**, 3466–3470.

42 X. Zhu, H. Sun, D. Yang, J. Yang, X. Li and X. Gao, Fabrication and characterization of X-ray array detectors based on polycrystalline PbI_2 thick films, *J. Mater. Sci.: Mater. Electron.*, 2014, **25**, 3337–3343.

43 C. Y. Chang, Y. C. Huang, C. S. Tsao and W. F. Su, Formation Mechanism and Control of Perovskite Films from Solution to Crystalline Phase Studied by in Situ Synchrotron Scattering, *ACS Appl. Mater. Interfaces.*, 2016, **8**, 26712–26721.

44 T. Zhang, M. Long, K. Yan, M. Qin, X. Lu, X. Zeng, C. M. Cheng, K. S. Wong, P. Liu, W. Xie and J. Xu, Crystallinity Preservation and Ion Migration Suppression through Dual Ion Exchange Strategy for Stable Mixed Perovskite Solar Cells, *Adv. Energy Mater.*, 2017, 1700118.

45 M. Yang, Z. Li, M. O. Reese, O. G. Reid, D. H. Kim, S. Siol, T. R. Klein, Y. Yan, J. J. Berry, M. F. A. M. van Hest and K. Zhu, Perovskite ink with wide processing window for scalable high-efficiency solar cells, *Nat. Energy*, 2017, **2**, 17038.

46 T. Kirchartz, F. Deledalle, P. S. Tuladhar, J. R. Durrant and J. Nelson, On the Differences between Dark and Light Ideality Factor in Polymer:Fullerene Solar Cells, *J. Phys. Chem. Lett.*, 2013, **4**, 2371–2376.

47 T. S. Sherkar, C. Momblona, L. Gil-Escrig, J. Ávila, M. Sessolo, H. J. Bolink and L. J. A. Koster, Recombination in Perovskite Solar Cells: Significance of Grain Boundaries, Interface Traps, and Defect Ions, *ACS Energy Lett.*, 2017, 1214–1222.

48 D. Yang, X. Zhou, R. Yang, Z. Yang, W. Yu, X. Wang, C. Li, S. F. Liu and R. Chang, Surface Optimization to Eliminate Hysteresis for Record Efficiency Planar Perovskite Solar Cells, *Energy Environ. Sci.*, 2016, **9**, 3071–3078.

49 T. Zhao, C.-C. Chueh, Q. Chen, A. Rajagopal and A. K. Y. Jen, Defect Passivation of Organic–Inorganic Hybrid Perovskites

by Diammonium Iodide toward High-Performance Photovoltaic Devices, *ACS Energy Lett.*, 2016, 757–763.

50 W. Nie, H. Tsai, R. Asadpour, J. C. Blancon, A. J. Neukirch, G. Gupta, J. J. Crochet, M. Chhowalla, S. Tretiak, M. A. Alam, H. L. Wang and A. D. Mohite, Solar cells. High-efficiency solution-processed perovskite solar cells with millimeter-scale grains, *Science*, 2015, **347**, 522–525.

51 D. Luo, L. Zhao, J. Wu, Q. Hu, Y. Zhang, Z. Xu, Y. Liu, T. Liu, K. Chen, W. Yang, W. Zhang, R. Zhu and Q. Gong, Dual-Source Precursor Approach for Highly Efficient Inverted Planar Heterojunction Perovskite Solar Cells, *Adv. Mater.*, 2017, **29**, 1604758.

52 G. Maculan, A. D. Sheikh, A. L. Abdelhady, M. I. Saidaminov, M. A. Haque, B. Murali, E. Alarousu, O. F. Mohammed, T. Wu and O. M. Bakr, $CH_3NH_3PbCl_3$ Single Crystals: Inverse Temperature Crystallization and Visible-Blind UV-Photodetector, *J. Phys. Chem. Lett.*, 2015, **6**, 3781–3786.